Dual functional catalytic materials of Ni over Ce-modified CaO sorbents for integrated CO_2 capture and conversion

Sun, H., Wang, J., Zhao, J., Shen, B., Shi, J., Huang, J., & Wu, C. (2019). Dual functional catalytic materials of Ni over Ce-modified CaO sorbents for integrated CO_2 capture and conversion. *Applied Catalysis B: Environmental*, *244*, 63-75. https://doi.org/10.1016/j.apcatb.2018.11.040

Published in:
Applied Catalysis B: Environmental

Document Version:
Peer reviewed version

Dual functional catalytic materials of Ni over Ce-modified CaO sorbents for integrated CO_2 capture and conversion

Hongman Sun[a], Jianqiao Wang[b], Jinhui Zhao[c], Boxiong Shen[b,*], Jeffrey Shi[c], Jun Huang[c,*] and Chunfei Wu[a,b,d,*]

[a] *School of Engineering and Computer Science, University of Hull, Hull, HU6 7RX, UK*

[b] *School of Energy and Environmental Engineering, Hebei University of Technology, Tianjin,300401, China*

[c] *School of Chemical and Biomolecular Engineering, the University of Sydney, Sydney, NSW 2037, Australia*

[d] *School of Chemistry and Chemical Engineering, Queen's University Belfast, Belfast, BT7 1NN, UK*

** Corresponding authors: E-mail: c.wu@hull.ac.uk (C. Wu); shenbx@hebut.edu.cn (B. Shen) jun.huang@sydney.edu.au (J. Huang).*

Abstract

Excessive anthropogenic CO_2 emission in the atmosphere is considered as one of the main contributions to the serious climate changes. However, with the growth of global economics, more fossil fuels will be consumed to feed the global activity, especially in developing countries. Thus, CO_2 needs to be captured for storage or converted to fuels or value-added chemicals. Herein, we propose and demonstrate a one-pot method synthesized dual functional materials (DFMs), which contain a sorbent coupled with a catalyst component, allowing the sorbent regeneration and CO_2 conversion to CO to perform simultaneously in a single reactor. This process requires no additional thermal energy for the regeneration of sorbents. In addition, CeO_2 is incorporated into the DFMs to largely enhance the stability of the materials for the process, and the influence of different Ce loadings on the performance of integrated CO_2 capture and conversion is studied. It is found that the DFMs with a Ca/Ni/Ce molar ratio of 1:0.1:0.033 displays an excellent CO yield (7.24 mmol g^{-1}) in the reverse water-gas shift (RWGS) reaction and a remarkable cyclic stability after 20 cycles of integrated CO_2 capture and conversion. Therefore, the incorporation of Ce into DFMs has two profits, for one thing, the oxygen vacancies generated by CeO_2 directly reduces the dissociated CO_2 regenerated from the DFMs, demonstrating the high CO yield; for another, the well-dispersed CeO_2, which could act as a physical barrier, effectively prevents the growth and agglomeration of CaO crystallite and NiO species.

Keywords: CO_2 capture and conversion, calcium looping, the reverse water-gas shift, dual functional materials, Ce-modified CaO sorbents

1. Introduction

Excessive anthropogenic CO_2 emission in the atmosphere is considered as one of the main contributions to the serious climate changes [1, 2]. The 21st conference on global warming (COP21) reached a landmark agreement (the Paris Agreement) to limit the increase of the global average temperature to 2.0 ˚C in 2100 [3]. To achieve such an objective made on the Paris Agreement, CO_2 emissions from energy- and industry-related sources must decrease dramatically after 2030 and reach net-zero levels between 2060 and 2080 [4]. There are a number of materials (e.g., amine-based solvents [5, 6], alkaline metal oxide-based sorbents [7, 8], ionic liquids [9, 10] and porous materials [11]) applicable for CO_2 capture from the use of fossil fuels. The carbon capture process usually relies on a temperature swing process for carbon capture and sorbent regeneration [12]. This process is energy intensive. Thus, considerable efforts have been devoted to developing more efficient and economical CO_2 capture technologies. Calcium-Looping (CaL) process based on the reversible carbonation/calcination reaction of CaO (Eq.1) has been applied for large-scale CO_2 capture from fossil fuel power plants [13-15] as originally proposed by Shimizu et al. [16] because of the high reactivity with CO_2 (theoretical capture capacity of CaO is 17.8 mmol g^{-1}) and the availability of low-cost natural CaO precursors [17-19]. The techno-economic modelling of CaL process has estimated that the carbon capture cost was $ 16-44 per ton CO_2, which is very competitive with the current amine scrubbing technologies costing about $ 32-80 per ton CO_2 [20, 21].

$$CaO + CO_2 \leftrightarrow CaCO_3, \Delta H_{r,298K} = -178\ \text{kJ mol}^{-1} \quad (1)$$

Currently, the great challenge of CaL process lies in the logistics and energy penalties of managing the concentrated CO_2, which must be transported to an underground injection facility (CCS) or a processing plant for conversion to useful products (CCU) [22, 23]. Compared to CCS, which is very expensive to run and could cause negative environmental impacts [24], CCU seems to be more attractive and promising due to CO_2 can be used as carbon source to offer an alternative to produce carbon-containing value-added products [25]. Thus, there is a growing interest in exploring the possibility of utilizing the captured CO_2 as a carbon feedstock and converting it to fuels or value-added chemicals [26-28].

Robert J. Farrauto's research group [22, 26] reported that using dual function materials (DFMs) for CO_2 capture and the conversion to synthetic natural gas at the same temperature (320 ˚C) simultaneously in the same reactor, requiring no additional heat input. The DFMs consisted of Ru as the methanation catalyst and nano-dispersed CaO as the CO_2 adsorbent. Both active sites were supported on a porous γ-Al_2O_3 carrier. A spillover process drove CO_2 from the sorbent to the Ru sites where methanation occurred using stored H_2 from excess renewable power. However, in this

process, the low loading of CaO (10 wt.%) resulted in a relatively low CO_2 capture capacity and consequent low methane yield. In addition, the main drawback of the mentioned process is the substantial utilization of noble metal Ru (10 wt.%), which can greatly increase the industrialization cost of such materials. In addition, Christoph Müller's research group [28] proposed and experimentally demonstrated a process that directly integrated CO_2 utilization (dry reforming of methane) into CO_2 capture allowing for the full conversion of the CO_2 captured. Importantly, a non-precious metal catalyst (Ni/MgO-Al_2O_3) and an inexpensive naturally occurring CO_2 sorbent (limestone) were utilized in this integrated process. This process is attractive economically and the coupled reactions are performed in a single reactor to avoid the transportation of solid sorbent which requires a strong mechanical strength of the sorbent in conventional CaL. However, the synthesis of materials consists of two discrete steps including the synthesis of dry reforming catalyst and the mixture of the catalyst with CO_2 capture sorbents, which is complex.

Another important product from the reduction of CO_2 is CO, which serves as a feedstock for producing chemicals and fuels via Fischer-Tropsch synthesis [29, 30]. The reverse water-gas shift (RWGS, Eq.2) is one of the most established reactions to convert CO_2 into the water and CO [31, 32], which can be exploited for introducing carbonyl functionalities into a plethora of molecules in both an academic and an industrial setting [33, 34].

$$CO_2 + H_2 \leftrightarrow CO + H_2O, \Delta H_{r,298K} = +41.2 \text{ kJ mol}^{-1} \quad (2)$$

However, the major challenge for the CaO-based sorbents and the Ni-based catalysts is the fast decay of CO_2 capture performance and the deactivation of catalytic performance with the number of cycles, respectively [35]. CeO_2, with a Tammann temperature of 1064 ˚C [36, 37], also has a possibility to be incorporated into CaO as a good inert material. Wang et al. synthesized a series of Ce-doped sorbents by a simple sol-gel method, and the sample (Ca/Ce = 15:1) showed a favourable capture capacity and cyclic stability, maintaining a CO_2 uptake capacity of 13.4 mmol g^{-1} after 18 cycles [36]. In addition, ceria exhibits excellent redox properties due to the rapid reduction of Ce^{4+} to Ce^{3+} associated with the creation of oxygen vacancies [38]. It has the ability to release oxygen under reducing atmosphere and storing oxygen under an oxidizing environment by filling oxygen vacancies [39]. The introduction of CeO_2 acting as a support to improve the catalytic activity has been studied extensively for the development of Ni-based catalysts [40-42]. Du et al. studied the catalytic properties of Ni/CeO_2 nanostructure for CO_2 reforming of methane and found that the strong metal-support effect can be helpful to prevent the sintering of Ni particles, reducing the deactivation of catalytic activity [40]. In addition, a series of Ni/CeO_2 catalysts with Ni loading ranging from 7 to 26 wt% were prepared via combustion synthesis and the stability was enhanced during methane dry reforming process [41]. Here, we propose and demonstrate a one-pot method to

synthesize DFMs, which contain a sorbent CaO coupled with a catalyst component Ni, as well as a physical barrier Ce, allowing the sorbent regeneration and CO_2 conversion to perform simultaneously in a single reactor via the reaction in Eq. (3).

$$CaCO_3 + H_2 \leftrightarrow CaO + CO + H_2O, \Delta H_{r,298K} = +219.2 \text{ kJ mol}^{-1} \quad (3)$$

The comparison between the conventional CaL process and the proposed process that integrates RWGS directly into CO_2 capture yielding a synthesis gas is shown in Fig. 1. Obviously, in the conventional CaL process as shown in Fig. 1a, two reactors including a carbonator and a calciner as well as the energy produced by the combustion are required for the cyclic performance of sorbents [43]. However, in this integrated process (Fig. 1b), both CO_2 capture and conversion are performed at the same temperature and a single reactor without an energy-intensive thermal swing process, eliminating the energy requirement, corrosion, and transportation issues associated with CCS. To the best of our knowledge, the simultaneous conversion of the captured CO_2 in a single reactor via the one-pot synthesized DFMs in the RWGS process has not been reported yet. In addition, the influence of different Ce loadings, as well as the mechanism on the performance of integrated CO_2 capture and conversion, were studied in details.

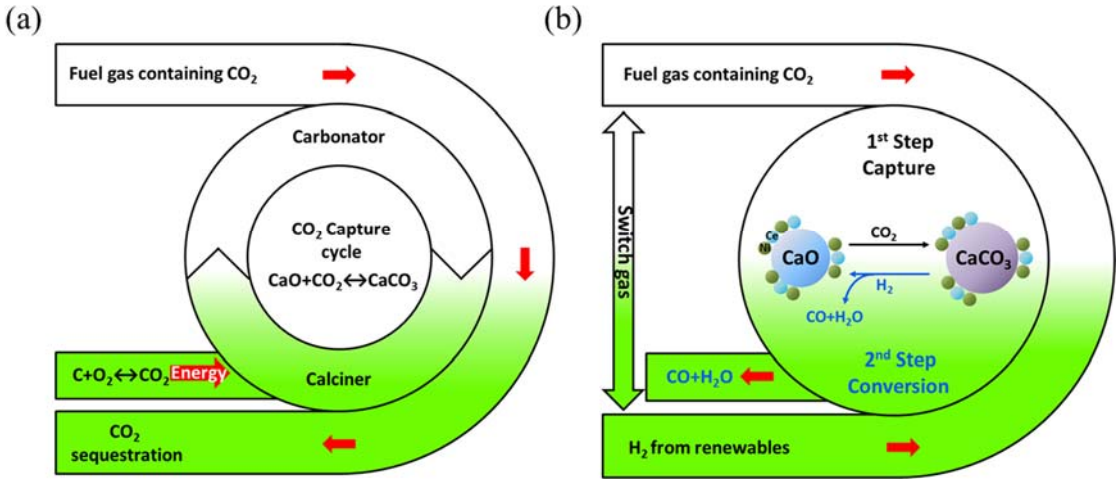

Fig. 1. Schematic diagram of (a) the conventional CaL process and (b) proposed process that integrates the RWGS process directly into the CO_2 capture process yielding a synthesis gas.

2. Experimental section

2.1. Dual functional materials preparation

All the DFMs were synthesized by a standard sol-gel combustion method reported by Santos et al. [44] and a typical synthesis process is as follows. Initially, predetermined amounts of analytical reagent-grade calcium nitrate tetrahydrate ($Ca(NO_3)_2 \cdot 4H_2O$, Sigma-Aldrich, 99.99%), nickel nitrate hexahydrate ($Ni(NO_3)_2 \cdot 6H_2O$, Sigma-Aldrich, 99.99%) and citric acid monohydrate (Sigma-

Aldrich, 99.99%) working as the chelation agent were added to distilled water at room temperature (water, citric acid and Ni^{2+} to Ca^{2+} molar ratios were 40:1, 1:1 and 0.1:1, respectively). Subsequently, for the Ce-doped DFMs, appropriate amounts of cerium nitrate hexahydrate ($Ce(NO_3)_2 \cdot 6H_2O$, Sigma-Aldrich, 99.99%) were added to the mixture solution and the Ce^{2+} to Ca^{2+} molar ratios were 1:60 and 1:30. Then, the mixture was continuously stirred at 80 ˚C to form a well-dispersed translucent pale green sol. The pale green sol was dried overnight at 130 ˚C. After drying, a low-density foam was obtained. The foam was easily crushed in a porcelain mortar and then calcined in a muffle furnace at 850 ˚C for 5 h with a heating rate of 2 ˚C min^{-1}. The obtained samples are designated as $Ca_1Ni_{0.1}$, $Ca_1Ni_{0.1}Ce_{0.017}$, and $Ca_1Ni_{0.1}Ce_{0.033}$, respectively. Pure sol-gel CaO was also prepared according to the same method used as the reference adsorbent.

2.2. Dual functional materials characterization

Elemental analyses of the catalysts were performed with a Perkin Elmer Optima 5300DV inductively coupled plasma optical emission spectrometer (ICP-OES) equipped with a Teflon sample introduction system. The sample was dissolved into the nitric acid and heated in the CEM MARS microwave system to 180 ˚C for 10 min and then cooled down to room temperature.

Powder X-ray diffraction (XRD) was performed on PANalytical empyrean series 2 diffractometer with Cu Kα radiation. The data was collected in the 5-80˚ 2θ range and analysed by X'pert Highscore plus software. Scherrer equation was used to estimate the average crystallite size based on the diffraction peaks at 42.2˚ of NiO particles and 28.5˚ of CeO_2 particles.

Nitrogen adsorption-desorption isotherms were measured using ASAP 2020 analyzer at 77 K. Brunauer-Emmett-Teller (BET) surface area was measured using the adsorption branch data in the relative pressure (P/P_0) range from 0.06 to 0.2, and the micropore volume (V_{micro}) was calculated by the t-plot method. The pore size distribution was calculated by the Barrett-Joyner-Halenda (BJH) method using nitrogen desorption branch data.

The surface morphology of samples was measured by a Stereoscan 360 Scanning electron microscopy (SEM) coupled with an energy dispersive X-ray spectrometer (EDX). The detailed structure of DFMs was characterized by transmission electron microscopy (TEM, a JEOL 2010) with an elemental mapping and high-resolution transmission electron microscopy (HRTEM, FEI talos F200). The preparation of samples for analysis involved being ultrasonically dispersed in absolute acetone and dropped cast on carbon-coated Cu grids.

The atomic concentrations of metals at the surface of the DFMs were determined by X-ray photoelectronic spectrometer (XPS, Thermo Fisher Scientific Escalab 250Xi) using Mg Kα radiation. The binding energies were calibrated using the C1s peak (284.6 eV) of adventitious

carbon. The ratios of Ce^{3+} to Ce^{4+} and Ni^{2+} to Ni^{3+} in DFMs were calculated using the deconvoluted Ce3d and Ni2p peak areas of the XPS spectra, respectively.

Raman spectroscopy (Thermo Scientific) was used to characterize the coke deposition. The Raman spectra were acquired in the range of 500-3500 cm^{-1} using a laser with a wavelength of 514.5 nm. The spectral resolution employed was 4 cm^{-1}.

2.3. Integrated CO_2 capture and conversion

A fixed-bed reactor coupled with a gas analyser operated under atmospheric pressure (as shown in Fig. S1) was used to determine the integrated CO_2 capture and conversion performance of the DFMs. Two sets of experiment were conducted to determine the influence of process parameters: the effect of different DMFs using CaO, $Ca_1Ni_{0.1}$, $Ca_1Ni_{0.1}Ce_{0.017}$ and $Ca_1Ni_{0.1}Ce_{0.033}$; the influence of carbonation and conversion temperatures of 650, 700, 750 °C. In a typical experiment, 250 mg powdered DFMs was loaded into the tube fixed by the quartz wool. The sample received a pre-reduction at 650 ˚C in a flow of 5% H_2 balanced with N_2 for 3 h with the heating rate of 10 ˚C min^{-1}. After reduction, the carbonation reaction was conducted in 15% CO_2 balanced with N_2 (100 mL min^{-1}) for 25 min. Subsequently, the DFMs were regenerated under 5% H_2 in N_2 (100 mL min^{-1}) after the fixed reactor was purged by N_2 for 5 min. With the further increase of temperature to 700 ˚C and then 750 ˚C, the carbonation reaction was carried out in 15% CO_2 balanced with N_2 (100 mL min^{-1}) for 25 min. After the fixed reactor was purged by N_2 for 5 min, the regeneration of DFMs was performed under 5% H_2 in N_2 (100 mL min^{-1}).

In-situ DRIFTs experiments were conducted by an FTIR spectrometer (JASCO-4600) coupled with a DRIFTs cell (Bruker). All spectra were recorded over accumulative 32 scans with a resolution of 4 cm^{-1} in the range of 4000-400 cm^{-1}. Prior to each experiment, the sample (~10 mg) was pre-reduced in 5% H_2 stream balanced with N_2 (100 ml min^{-1}) at 650 °C for 30 min. And then the carbonation was performed in 15% CO_2 balanced with N_2 for 25 min. Subsequently, the DFMs were regenerated under 5% H_2 in N_2 (100 mL min^{-1}) after the in-situ reactor was purged by N_2 for 5 min.

2.4. Cyclic CO_2 capture and conversion tests

Cyclic CO_2 capture and conversion performance of DFMs was conducted in a fixed-bed reactor coupled with a gas analyser under atmospheric pressure (as shown in Fig. S1). Approximately 250 mg of powdered DFMs was loaded into the tube fixed by the quartz wool. The sample received a pre-reduction at 650 ˚C in a flow of 5% H_2 balanced with N_2 for 3 h with the heating rate of 10 ˚C min^{-1}. Subsequently, the carbonation reaction was conducted in 15% CO_2 balanced with N_2 (100 mL min^{-1}) for 25 min. After carbonation, the DFM was regenerated under 5% H_2 in N_2 (100 mL

min^{-1}) after the fixed reactor was purged by N_2 for 3 min. In total, 20 cycles of the integrated CO_2 capture and conversion process were performed.

3. Results and Discussion

3.1. Characterization of fresh dual functional materials

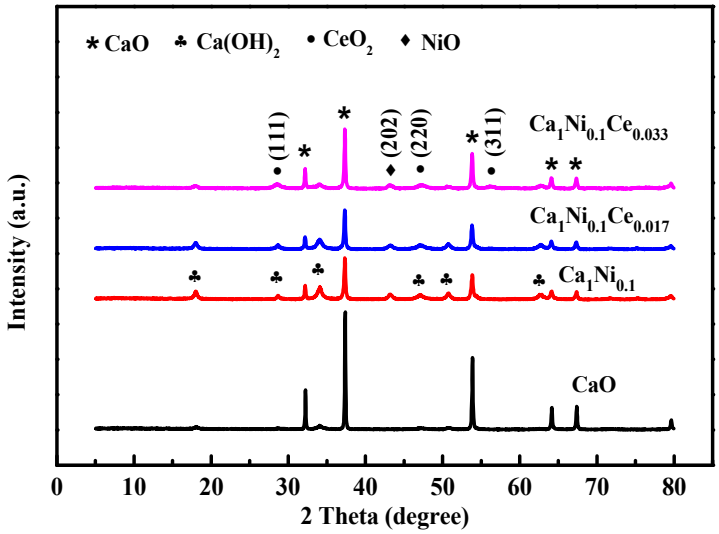

Fig. 2. XRD patterns of fresh DFMs.

Table 1 Elemental analysis, average crystallite size and textural properties and of fresh DFMs.

Samples	Molar ratio[a]			NiO[b]	CeO_2[b]	S_{BET}[c]	V_p[d]
	Ca	Ni	Ce	(nm)	(nm)	(m^2 g^{-1})	(cm^3 g^{-1})
CaO	1	0	0	n.a.	n.a.	38.5	0.15
$Ca_1Ni_{0.1}$	1	0.10	0	15	n.a.	12.8	0.11
$Ca_1Ni_{0.1}Ce_{0.017}$	1	0.09	0.016	12	8	22.5	0.20
$Ca_1Ni_{0.1}Ce_{0.033}$	1	0.10	0.032	12	8	20.7	0.14

[a] Molar ratios normalized with Ca=1 measured by ICP

[b] Average crystallite size calculated by Scherrer equation

[c] BET surface areas

[d] Total pore volume measured at a relative pressure (P/P_0) of 0.99

ICP-OES is used to obtain elemental analysis data for DFMs, and the results are shown in Table 1. The atomic ratio of Ni to Ca are around 0.1 for all the DFMs, which is inconsistent with the predetermined metal contents. As for $Ca_1Ni_{0.1}Ce_{0.017}$ and $Ca_1Ni_{0.1}Ce_{0.033}$, the atomic ratios of Ce to Ca are 0.017 and 0.032, respectively, which are used for the investigation of the influence of Ce loadings on integrated CO_2 capture and conversion.

The XRD patterns of fresh DFMs are presented in Fig. 2. The results evidence the presence of CaO in fresh samples, along with low-intensity peaks of $Ca(OH)_2$. It is attributed to the reaction between CaO powder and moisture in the cooling process of calcination and storage. After the incorporation of Ni, the DFMs exhibit a diffraction peak at 2θ=43.2˚, indicating the characteristic peak of NiO (2 0 2) [45]. The average crystallite size corresponding to NiO phase is calculated as 15, 12, and 12 nm for $Ca_1Ni_{0.1}$, $Ca_1Ni_{0.1}Ce_{0.017}$, and $Ca_1Ni_{0.1}Ce_{0.033}$, respectively. Therefore, it is concluded that CeO_2, considered as a physical barrier, prevented the growing and agglomeration of the NiO crystallite and led to the decrease of the average crystallite size of NiO, which has been reported in other literature [46]. According to the Scherrer equation, the sharp and broad diffraction peaks are related to the large and small average crystallite size, respectively [47]. So the broad diffraction peak at 28.5˚ in $Ca_1Ni_{0.1}Ce_{0.033}$ is corresponding to CeO_2 instead of $Ca(OH)_2$ due to the large crystallite size property of $Ca(OH)_2$. In addition, the appearance of diffraction peaks at 47.3 and 56.3 ˚ pertaining to CeO_2 crystallite phase is also obvious in the Ce-doped samples.

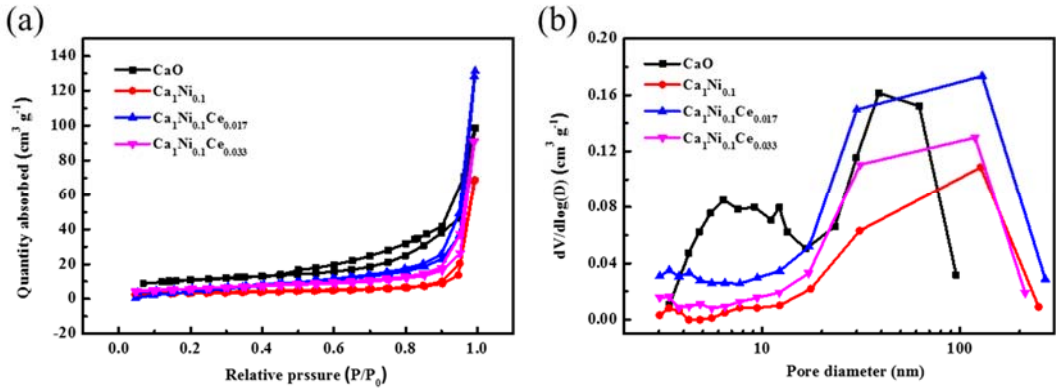

Fig. 3. (a) N_2 adsorption-desorption isotherms and (b) pore size distribution calculated from the BJH desorption branch.

N_2 adsorption-desorption isotherms and pore size distributions are conducted to determine the structure of the DFMs (Fig. 3). Textural properties derived from different DFMs are summarised in Table 1. All the isotherms obtained for DFMs exhibit a type IV isotherm shape. The shape of the hysteresis loops for all DFMs is type H3 resulting from the slit-shaped pores generated by the addition of citric acid. The surface area (12.75 m^2 g^{-1}) and pore volume (0.106 cm^3 g^{-1}) of $Ca_1Ni_{0.1}$ are lower than those of the reference sol-gel CaO (38.51 m^2 g^{-1} and 0.153 cm^3 g^{-1}, respectively) due to the introduction of NiO particles. With the doping of Ce, the BET surface area and pore volume are slightly increased. The BJH pore size distribution (Fig. 3b) indicates the formation of pores smaller than 4 nm in $Ca_1Ni_{0.1}Ce_{0.017}$ and $Ca_1Ni_{0.1}Ce_{0.033}$ and the disappearance of the mesopores ranging from 4 nm to 10 nm.

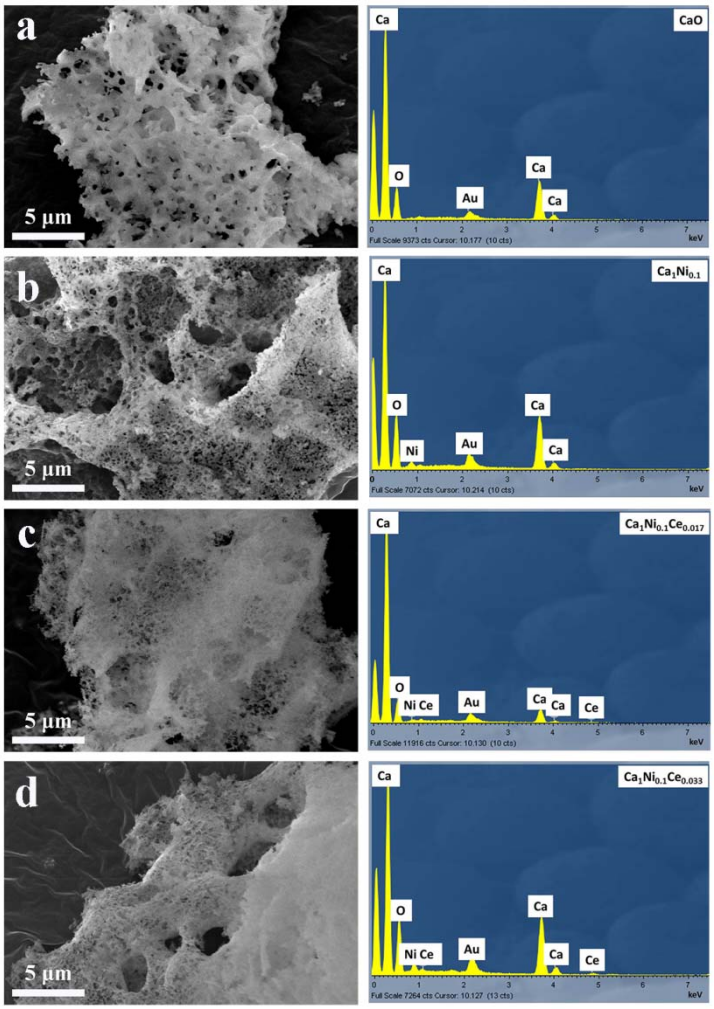

Fig. 4. SEM images and EDX of fresh DFMs (a) CaO, (b) $Ca_1Ni_{0.1}$, (c) $Ca_1Ni_{0.1}Ce_{0.017}$, (d) $Ca_1Ni_{0.1}Ce_{0.033}$.

The morphologies and active components of the fresh DFMs are determined by SEM-EDX analysis, as shown in Fig. 4. In the calcination process of DFMs preparation using the sol-gel method, a large amount of gas and heat would release during the reaction and enhance the formation of a porous and fluffy structure [48]. Therefore, it can be observed in Fig. 4a that the synthesized sol-gel CaO possesses a fluffy and porous structure, which is in agreement with the pore size distribution in Fig. 3b. After the introduction of NiO into the adsorbents, a peak belonging to Ni is observed in the EDX results and the surface of the DFMs become loose, which is favorable for the reaction between CaO and CO_2. The morphologies of the CeO_2-doped DFMs are much different from others, appearing as a more loose structure with lots of micropores and mesopores. This morphology can contribute to the excellent cyclic performance of CO_2 capture due to the efficient diffusion of CO_2 inward in the sorbent and reacts with CaO in the interior and exterior of the sorbent at the same time [49]. In the carbonation process, there exists a critical product layer thickness of $CaCO_3$, at which

the reaction transforms from the kinetic-controlled stage of carbon capture to the diffusion-controlled stage [50]. When the product layer thickness achieves this critical value, there is more CaO reacting with CO_2 for the Ce-doped DFMs. In addition, the EDX results show a small peak assigned to Ce in Fig. 4c and Fig. 4d indicating the successful incorporation of Ce into DFMs. It is noted that doping cerium can bring a large number of oxygen vacancies and an improved oxygen transport capacity ($Ce^{3+} \leftrightarrow Ce^{4+}$) [51, 52]. The oxygen vacancy is favorable to the diffusion of CO_2 and the mobility of O^{2-} according to the proposed adsorption mechanism of CO_2 [53]. The process is shown as follows:

$$CO_2\ (g) \rightleftharpoons (CO_2)_{ads} \quad (4)$$

$$(CO_2)_{ads} + O^{2-} \rightarrow CO_3^{2-} \quad (5)$$

$$CO_3^{2-} + CaO \rightarrow CaCO_3 + O^{2-} \quad (6)$$

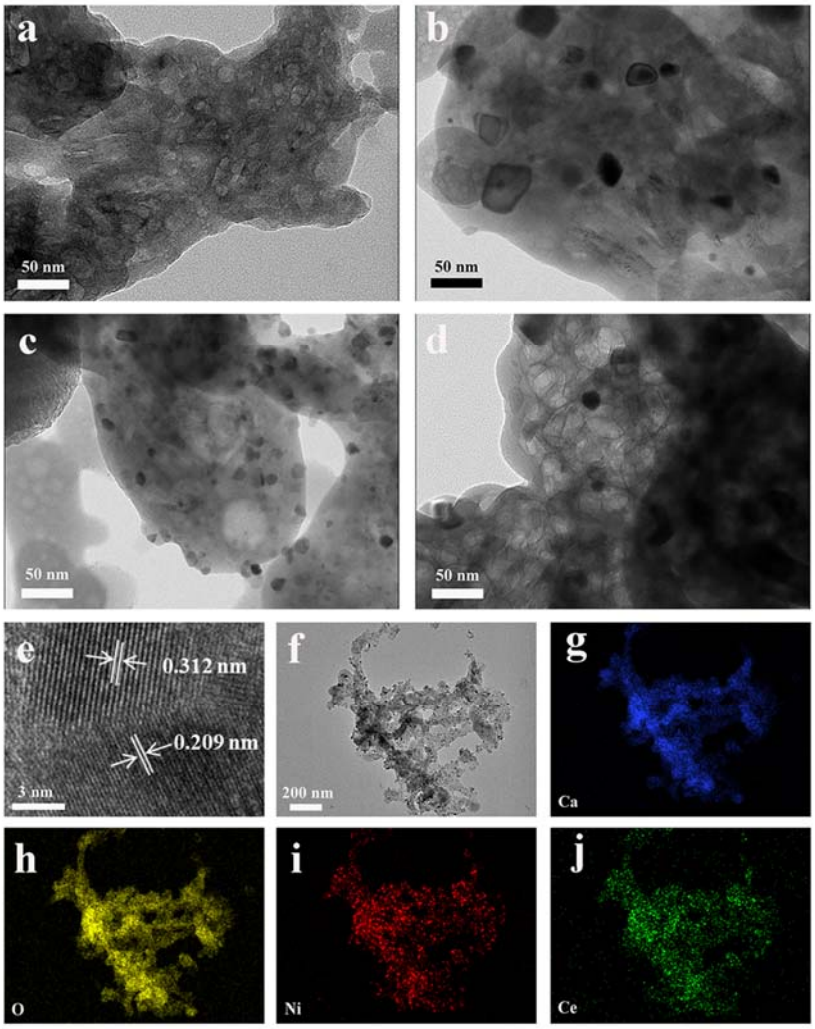

Fig. 5. TEM images of fresh DFMs (a) CaO, (b) $Ca_1Ni_{0.1}$, (c) $Ca_1Ni_{0.1}Ce_{0.017}$, (d) $Ca_1Ni_{0.1}Ce_{0.033}$. High-resolution TEM (e) and elemental mappings (f-i) of $Ca_1Ni_{0.1}Ce_{0.033}$.

The porous structure and particle distribution are shown in Fig. 5. The pure sol-gel CaO as shown in Fig. 5a exhibits a porous structure without apparent particles, which is in agreement with the SEM results. There are irregular particles distributed on the sol-gel CaO matrix, which are assigned to NiO particles as shown in Fig. 5. As for the Ce-doped DFMs, the metal particle size exhibits a dramatic decrease. It is verified that nano-sized particles with the more coordinative unsaturated sites on the surfaces are easier to absorb CO_2, and they enable faster diffusion rate of CO_2 through the layer of formed $CaCO_3$ [54, 55]. With further increase of Ce loading, the $Ca_1Ni_{0.1}Ce_{0.033}$ displays the obvious lattice fringes (Fig. 5e) indicating the high crystallinity of CeO_2 and NiO. The interplanar spacing of 0.312 nm and 0.209 nm represent (111) lattice plane of CeO_2 and (202) lattice plane of NiO, respectively. The elemental mapping of $Ca_1Ni_{0.1}Ce_{0.033}$ demonstrates the uniform distribution of Ca, O, Ni and Ce elements, which is effective to delay the sintering and prevent the aggregation of CaO particles, resulting in an outstanding stability.

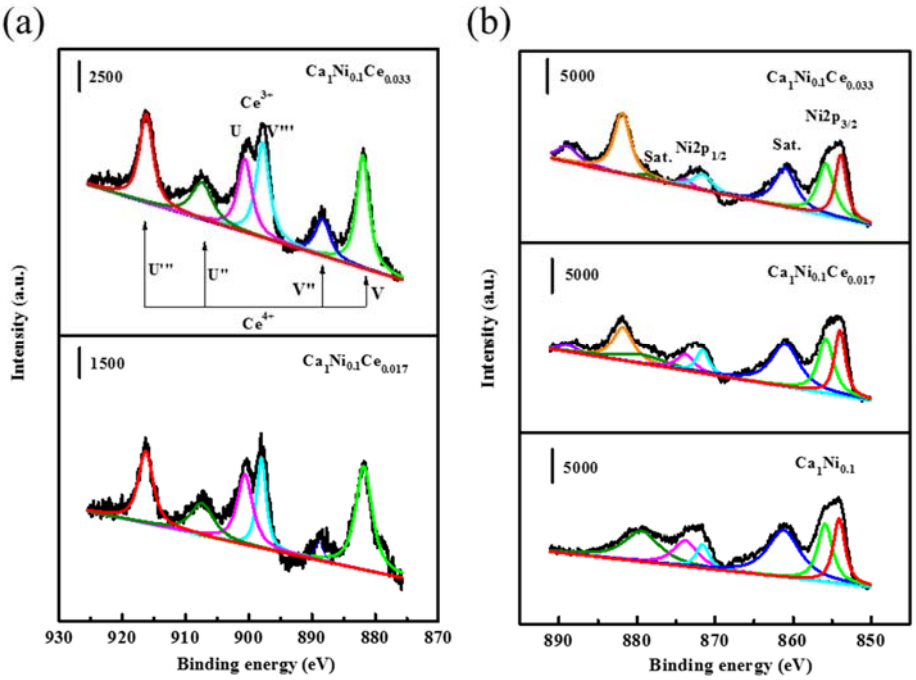

Fig. 6. XPS spectra of (a) Ce3d and (b) Ni2p of fresh DFMs.

Table 2 XPS results of DFMs

Samples	Ce^{3+}/Ce^{4+}	Ni^{2+}/Ni^{3+}
CaO	/	/
$Ca_1Ni_{0.1}$	/	0.72
$Ca_1Ni_{0.1}Ce_{0.017}$	0.52	0.90
$Ca_1Ni_{0.1}Ce_{0.033}$	0.58	1.10

XPS analysis is performed on DFMs to identify the valence states and the chemical composition. The Ce3d spectra are complicated due to the existence of two different cerium oxidation states, the hybridization of the O2p valance band with the Ce4f level as well as spin-orbit coupling [53]. The main features of the Ce3d are composed of ten peaks marked as u and v, which are corresponding to five pairs of spin-orbit components attributed to $3d_{3/2}$and $3d_{5/2}$ [56, 57]. Six of the peaks labelled as U, U″, U‴, V, V″, V‴ are associated to Ce^{4+} ions, and the other four peaks denoted by U^0, U′, V^0, V′ are connected to Ce^{3+} ions. As shown in Fig. 6a, six main binding energy peaks can be observed including 916.3, 907.4, 888.9 and 881.8 eV assigned to $Ce^{4+}3d_{5/2}$, as well as 900.6 and 898.0 eV ascribed to $Ce^{3+}3d_{3/2}$. Therefore, Ce mainly exists in +3 and +4 oxidation states in the DFMs. The Ce^{3+} to Ce^{4+} ratios of the $Ca_1Ni_{0.1}Ce_{0.017}$ and the $Ca_1Ni_{0.1}Ce_{0.033}$ are 0.52 and 0.58, respectively, indicating more oxygen vacancies created by the Ce^{3+} with the increase of Ce loading.

By using a Gaussian fitting method, the Ni2p spectrum (Fig. 6b) is fitted by considering two spin-orbit doublet characteristic of Ni^{2+} and Ni^{3+} and two shakeup satellites [58]. According to the fitting data, the fitting peaks at the binding energy of 854.1 and 871.6 eV are indexed to Ni^{2+}, while the fitting peaks at the binding energy of 855.8 and 873.8 eV are ascribed to Ni^{3+} [59]. In addition, the satellite peaks at 861.0 eV and 879.4 eV are two shake-up type peaks of Ni at the high binding energy side of the $Ni2p_{3/2}$ and $Ni2p_{1/2}$ edge, respectively [60]. Two peaks at 881.8 and 888.9 eV of both $Ca_1Ni_{0.1}Ce_{0.017}$ and $Ca_1Ni_{0.1}Ce_{0.033}$ are caused by the introduction of Ce. Compared to the $Ca_1Ni_{0.1}$, the Ni^{2+} to Ni^{3+}ratios of the $Ca_1Ni_{0.1}Ce_{0.017}$ and $Ca_1Ni_{0.1}Ce_{0.033}$ are increased to 0.90 to 1.10, respectively, due to the reducing properties of Ce^{3+} as shown in Eq. (7). Besides, the binding energies of $Ca2p_{1/2}$ and $Ca2p_{3/2}$ as shown in Fig. S2a exhibit a separation of 3.5 eV and an intensity ratio of 1/2, indicating the existing of Ca^{2+} [56]. Fig. S2b displays the high resolution spectrum for O1s, which exhibits three different peaks (marked as O1, O2, and O3), corresponding to the metal oxygen bonds (O1, ~529.5 eV), oxygen ions (O2, ~531.2 eV) and physic or chemisorbed water at or within the surface (O3, ~533.1 eV) [58]. Based on these analyses, the surface of as-prepared DFMs possesses a composition containing Ni^{2+}, Ni^{3+}, Ca^{2+}, and O^{2-}.

$$Ce^{3+} + Ni^{3+} \rightarrow Ce^{4+} + Ni^{2+} \quad (7)$$

3.2. Integrated CO_2 capture and conversion performance

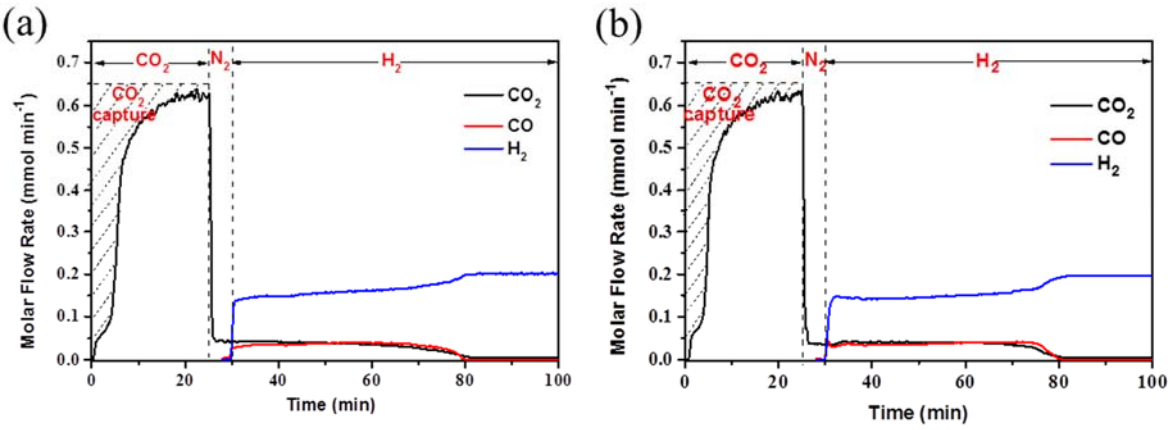

Fig. 7. Integrated CO_2 capture and conversion reactions at 650 ˚C of (a) $Ca_1Ni_{0.1}$; (b) $Ca_1Ni_{0.1}Ce_{0.033}$.

Table 3 The CO_2 capture capacity, CO_2 and CO yields, as well as turnover frequency (TOF) of different DFMs at 650 ˚C.

Samples	Capture capacity[a] mmol g^{-1}	CO_2 yield[a] mmol g^{-1}	CO yield[a] mmol g^{-1}	Carbon Balance (%)	CO_2 conversion (%)	TOF[b] s^{-1}
CaO	15.7	7.6	3.2	68.4	23.4	/
$Ca_1Ni_{0.1}$	15.0	7.2	6.9	94.4	46.0	0.72
$Ca_1Ni_{0.1}Ce_{0.017}$	14.2	6.8	7.2	98.0	50.7	0.75
$Ca_1Ni_{0.1}Ce_{0.033}$	14.1	6.7	7.3	99.2	51.8	0.78

[a] calculated by per gram of sorbents

[b] $\mathrm{TOF} = \frac{r_{AC}}{n_{OF}} = \frac{n_{\text{conversion per gram of sorbent per second}}}{n_{\text{total metal}} \times \text{Ni dispersity}}$

The integrated CO_2 capture and conversion performances of DFMs are depicted in Fig. 7. The difference between the recorded CO_2 concentrations in the outlet gas stream during CO_2 capture stage and a blank experiment (as shown in Fig. S3, i.e., without any CO_2 sorbent) is equal to the capacity of CO_2 captured. The CO_2 capture capacity, CO_2 and CO yields, as well as the TOF derived from different DFMs, are summarised in Table 3. The capture capacity of the synthesized CaO is determined as 15.68 mmol g^{-1} in the first step, which is much higher than that reported in the previous literature due to the porous structure generated by the sol-gel method [61, 62]. In the second step, a flow of 100 ml min^{-1} of 5% H_2 balanced with N_2, ensuring a ratio of H_2 to CO_2 over 3:1, is used. Only a small amount of CO (3.16 mmol g^{-1}) is observed in Fig. S4a for the synthesized CaO due to the absence of Ni active sites, while the majority of captured CO_2 (7.56 mmol g^{-1})) is released through the regeneration of the DFMs in the H_2 atmosphere. The CO2 conversion is only

23.4% without the introduction of Ni and Ce species. The unreleased CO_2 is proposed to be contained inside the synthesized CaO as the regeneration temperature is the same as capturing temperature.

After the incorporation of Ni, CO_2 capture capacity is slightly decreased due to the reduced mass content of CaO in the DFMs and CO yield is dramatically increased to 6.88 mmol g^{-1} as shown in Fig. 7a indicating that the addition of Ni can promote the reaction of Eq. (3) in a positive direction through the reaction of CO_2 and H_2. After the incorporation of Ce with a Ca/Ce molar ratio of 1:0.017, the CO yield is slightly increased in Fig. S4b because of the small amount doping of Ce. Further increasing the loading of Ce, $Ca_1Ni_{0.1}Ce_{0.033}$ (Fig. 7b) exhibits the best integrated CO_2 capture and conversion performance with a highest CO yield (7.24 mmol g^{-1}) and a relatively lower CO_2 yield (6.70 mmol g^{-1}). The highest TOF of the $Ca_1Ni_{0.1}Ce_{0.033}$ is 0.780 s^{-1} indicating a promising catalytic activity of the $Ca_1Ni_{0.1}Ce_{0.033}$ due to the enhanced oxygen storage capacity of Ca-Ce promoted the catalytic performance of Ni species. The $Ca_1Ni_{0.1}Ce_{0.033}$ exhibited the highest CO_2 conversion of 51.8% coupled with a nearly 100% CO selectivity, which is much better than the performance reported by Ranjbar et al. (CO_2 conversion and CO selectivity are 38% and 95%, respectively at 650 ˚C with 10% Ni loading) [63] and Wang et al. (CO_2 conversion and CO selectivity are 38% and 100%, respectively at 600 ˚C with 10% Co loading) [64]. The detailed comparison of integrated CO_2 capture and conversion and reported in the literature are summarised in Table S1. It was found compared the conversional RWGS reaction, the performance of integrated CO_2 capture and conversion proposed in this work exhibited a good CO_2 conversion and a remarkable CO selectivity, as well as a good stability.

To date, two main reaction mechanisms have been proposed: a redox process (Scheme 1) [65-67] and an associative "formate" mechanism (Scheme 2) [68-70].

Scheme 1:

$$CO_2 + Ni \leftrightarrow CO + Ni^{2+} \quad (8)$$

$$H_2 + Ni^{2+} \leftrightarrow H_2O + Ni \quad (9)$$

$$CO_2 + Ce^{3+} \leftrightarrow CO + Ce^{4+} \quad (10)$$

$$H_2 + Ce^{4+} \leftrightarrow H_2O + Ce^{3+} \quad (11)$$

Scheme 2:

$$H_2 + 2\sigma \leftrightarrow 2H_{ad} \quad (12)$$

$$CO_2 + \sigma \leftrightarrow CO_{2,ad} \quad (13)$$

$$CO_{2,ad} + H_{ad} \leftrightarrow HCOO_{ad} + \sigma \quad (14)$$

$$HCOO_{ad} + \sigma \leftrightarrow CO_{ad} + OH_{ad} \quad (15)$$

$$H_{ad} + OH_{ad} \leftrightarrow H_2O + 2\sigma \quad (16)$$

$CO_{ad} \leftrightarrow CO + \sigma$ (17)

In the redox mechanism, the interaction of CO_2 over oxygen vacancy results in the oxidation of catalyst and release of CO molecule. The oxidized catalyst is subsequently reduced by H_2. In the associative mechanism, σ refers to sites on the oxide support. The main reaction intermediate is a bidentate formate, which decomposes to form CO and terminal hydroxyl groups. As shown in Fig. 8 and Fig. S5, the in-situ DRIFTS spectra show peaks around 1780 and 2120 cm^{-1} corresponding to the carbonyl, which is caused by the stretching mode of CO molecules bound at on-top metal sites. The characteristic peaks around 2450, 2850 and 2950 cm^{-1} are assigned to the formate species, indicating the co-existence of Scheme 1 and 2. The spectra of the $Ca_1Ni_{0.1}$ and $Ca_1Ni_{0.1}Ce_{0.033}$ in Fig. 8 are quite similar to the spectra of CaO and $Ca_1Ni_{0.1}Ce_{0.017}$ in Fig. S5. However, the performance of integrated CO_2 capture and conversion exhibits a great difference between various DFMs. Thus, we propose that the surface formate and carbonyl observed by DRIFTS were not the main reaction intermediates for the formation of CO, which has also been reported by Alexandre et al. [71]. Thus, a model for the reaction mechanism of the integrated CO_2 capture and conversion over DFMs is proposed in Fig. 9. As for the DFMs without cerium doping, after switching the gas to H_2, CO_2 will spillover from the surface of the DFMs and react with Ni active sites resulting in the formation of CO and NiO (Eq. (8)). The reduction of NiO by the adsorbed H_2 species is proposed by Eq. (6). In this case, Ni^{2+} becomes Ni and the oxygen reacts with hydrogen to form water. Ce^{3+} and Ce^{4+} represent reduced ceria (oxygen vacancy) and oxidized ceria, respectively. After the incorporation of cerium, the first step involves the interaction of CO_2 over oxygen vacancy resulting in the oxidation of catalyst and release of CO molecule as represented by Eq. (10). The adsorbed H_2 species extracts lattice oxygen from ceria, giving out H_2O molecule along with the reduction of catalyst (Eq. (11)).

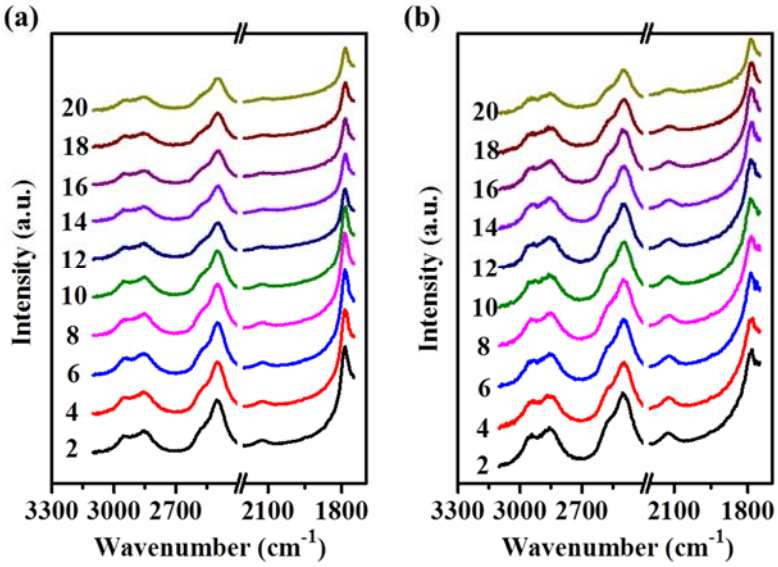

Fig. 8. In-situ DRIFTS spectra of the species formed over (a) $Ca_1Ni_{0.1}$; (b) $Ca_1Ni_{0.1}Ce_{0.033}$ after switching gas to H_2 for 2, 4, 6, 8, 10, 12, 14, 16, 18 and 20 min.

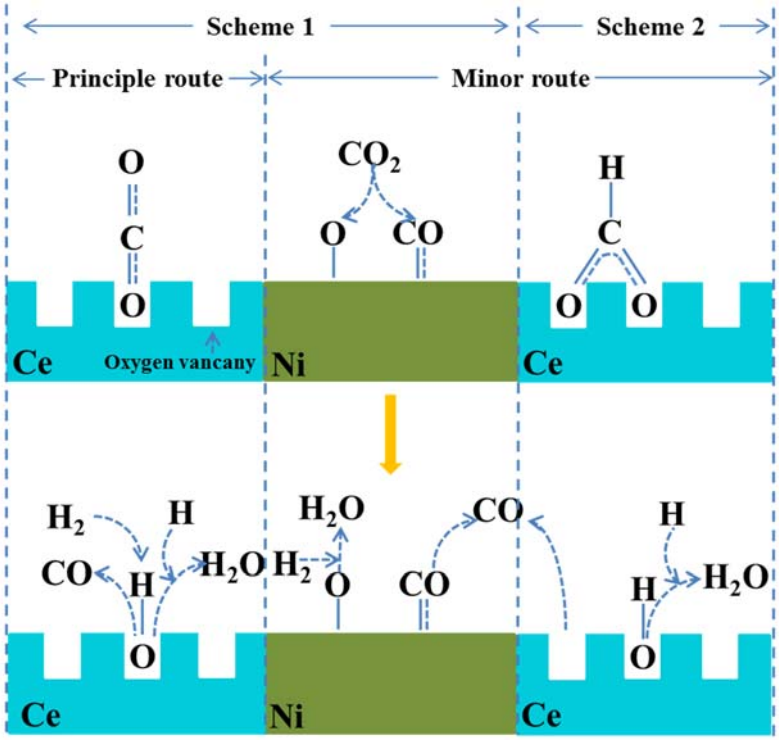

Fig. 9. Reaction mechanism of the RWGS reaction over DFMs.

The influence of reaction temperature was studied using the $Ca_1Ni_{0.1}Ce_{0.033}$ catalyst. When increasing the carbon capture and conversion temperature from 650 to 700 and further to 750 ˚C, as shown in Fig. S6, it is found that the decomposition rate of $CaCO_3$ is dramatically increased after switching to H_2. However, the rate of the RWGS reaction is marginally increased due to the controlling step of CO_2 conversion with limited active Ni species. Therefore, 650 ˚C is optimal for carbon capture and CO production in this work.

3.3. Cyclic CO_2 capture and conversion performance

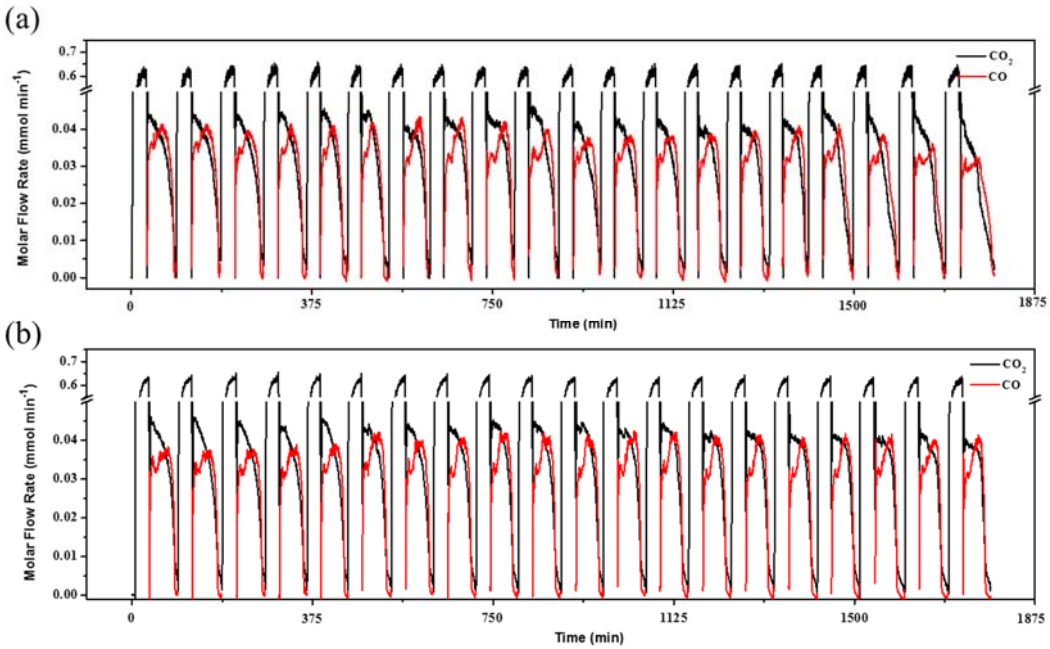

Fig. 10. Cyclic CO_2 capture and conversion reactions of (a) $Ca_1Ni_{0.1}$; (b) $Ca_1Ni_{0.1}Ce_{0.033}$.

The cyclic performance of the integrated CO_2 capture and conversion of DFMs with the doping of Ce is evaluated by 20 cycles and the experimental results are presented in Fig. 10. The $Ca_1Ni_{0.1}$ shows an initial CO released capacity of 6.88 mmol g^{-1}; however, the CO released capacity is reduced rapidly with increasing cycle numbers, dropping to about 4.62 mmol g^{-1} at the 20^{th} cycle. This decay of carbonation conversion over repeated cycles is attributed to the agglomeration and sintering of unsupported CaO and the carbon deposition of the Ni-based catalyst. However, it shows that the integrated CO_2 capture and conversion performance of $Ca_1Ni_{0.1}Ce_{0.033}$ is kept completely unchangeable after 20 cycles due to the doping of CeO_2. The decay of CO_2 conversion in the $Ca_1Ni_{0.1}$ is not caused by the deposited carbon on the active sites due to no peak can be observed in the Raman spectra in Fig. S7.

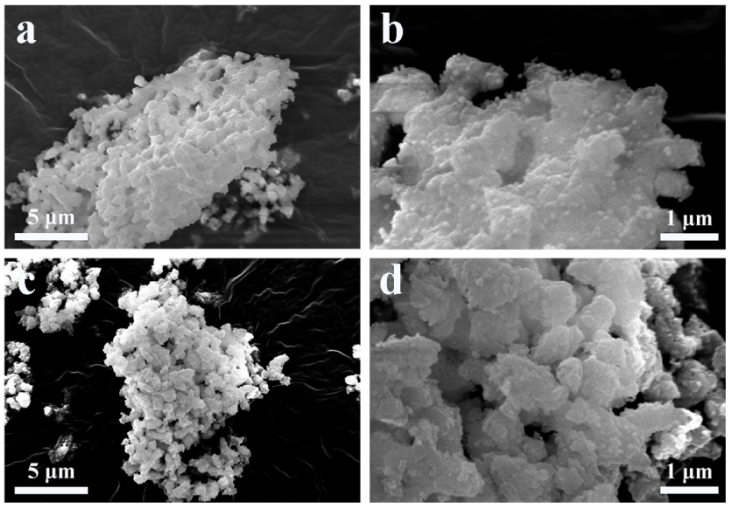

Fig. 11. SEM images of DFMs after 20 cycles of integrated CO_2 capture and conversion (a) and (b) $Ca_1Ni_{0.1}$, (c) and (d) $Ca_1Ni_{0.1}Ce_{0.033}$.

Fig. 11 displays the SEM images of DFMs after 20 cycles of integrated CO_2 capture and conversion. By comparing the porous structure, the obvious changes can be observed between the spent $Ca_1Ni_{0.1}$ and $Ca_1Ni_{0.1}Ce_{0.033}$. As for the $Ca_1Ni_{0.1}$, the porous structure is almost disappeared and the surface morphology is changed into a bulk structure, indicating the sintering of CaO particles and Ni active sites, which is in agreement with the performance after 20 cycles of integrated CO_2 capture and conversion. However, a porous structure is observed for the $Ca_1Ni_{0.1}Ce_{0.033}$ after 20 cycles of integrated CO_2 capture and conversion due to the doping of CeO_2 acting as a support of DFMs. This porous structure can also be confirmed by the N_2 adsorption-desorption isotherms and pore size distribution in Fig. S8. Thus, the Ce-doped DFMs exhibited an excellent stability in the integrated CO_2 capture and conversion.

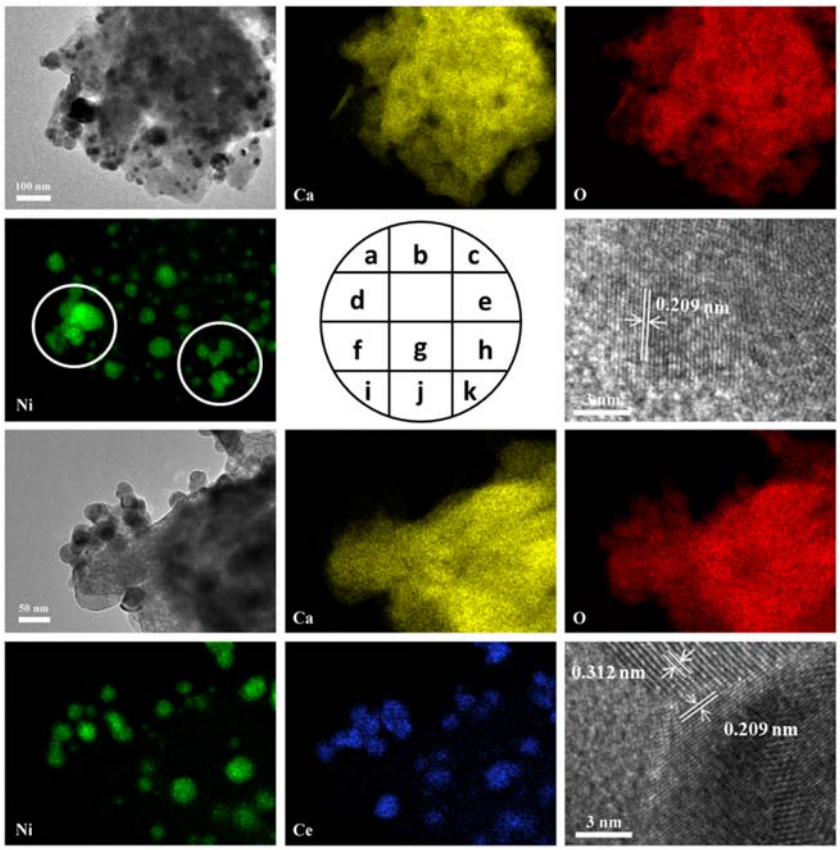

Fig. 12. TEM, elemental mappings and high-resolution TEM images of DFMs after 20 cycles of integrated CO_2 capture and conversion (a-e) $Ca_1Ni_{0.1}$, (f-k) $Ca_1Ni_{0.1}Ce_{0.033}$.

The porous structure and particles distribution of DFMs after 20 cycles of integrated CO_2 capture and conversion are characterized by TEM and HRTEM, as presented in Fig. 12. It is evident that the porous structure of $Ca_1Ni_{0.1}$ is almost disappeared and the Ni element mapping exhibits an agglomeration, which is in agreement with the SEM images. In addition, the metal particle size of $Ca_1Ni_{0.1}$ after 20 integrated cycles is dramatically increased as shown in Fig. S9. The exposed planes are (202) planes of NiO with an interplanar spacing of 0.209 nm calculated from the corresponding HRTEM images. After the incorporation of Ce, the $Ca_1Ni_{0.1}Ce_{0.033}$ still exhibits a porous structure with a uniform distribution of Ni element after 20 integrated cycles and the metal particle size is slightly increased due to the CeO_2 acting as a physical barrier to prevent the aggregation of Ni active sites. The interplanar spacing of 0.312 nm and 0.209 nm represent (111) lattice plane of CeO_2 and (202) lattice plane of NiO, respectively.

4. Conclusions

The CO_2 capture and conversion process integrating the RWGS directly into CO_2 capture is proposed using a one-pot method synthesized DFMs, which contain a sorbent coupled with a catalyst component. In this integrated process, the sorbent regeneration and CO_2 conversion are performed simultaneously in a single reactor, requiring no additional heat input. The synthetic natural gas can be recycled to an industrial facility, conserving fuel while reducing CO_2 emissions. It is found that with the incorporation of CeO_2, the DFMs exhibited an outstanding CO yield (7.24 mmol g^{-1}) and the highest TOF value (0.780 s^{-1}) due to the dissociated CO_2 can be directly oxidized by the oxygen vacancies generated by the ceria support. In addition, the dissociated CO_2 and hydrogen over nickel surface can directly form CO and supply spillover hydrogen to nearby oxygen vacancies, respectively. After 20 cycles of integrated CO_2 capture and conversion, the Ce-doping DFMs exhibit an excellent stability due to the well-dispersed CeO_2, which could act as a physical barrier, effectively prevents the growth and agglomeration of CaO crystallite and NiO species.

Acknowledgements

The authors are grateful for the financial support of National Natural Science Foundation of China (no. 21706050), SOAR Fellowship at the University of Sydney and China Scholarship Council (CSC, no. 201606450016).

Reference

[1] IPCC, Climate change 2014: mitigation of climate change, Cambridge University Press, 2015.
[2] E. Haque, M.M. Islam, E. Pourazadi, S. Sarkar, A.T. Harris, A.I. Minett, E. Yanmaz, S.M. Alshehri, Y. Ide, K.C.W. Wu, Chem-Asian J. 12 (2017) 283-288.
[3] C.J. Rhodes, Science Progress 99 (2016) 97-104.
[4] J. Rogelj, M. den Elzen, N. Höhne, T. Fransen, H. Fekete, H. Winkler, R. Schaeffer, F. Sha, K. Riahi, M. Meinshausen, Nature 534 (2016) 631.
[5] B. Mandal, S. Bandyopadhyay, Chem. Eng. Sci. 61 (2006) 5440-5447.
[6] A.L. Chaffee, G.P. Knowles, Z. Liang, J. Zhang, P. Xiao, P.A. Webley, Int. J. Greenh. Gas Con. 1 (2007) 11-18.
[7] C. Zhao, X. Chen, C. Zhao, Energ. Fuel. 24 (2010) 1009-1012.
[8] Y. Liang, D. Harrison, R. Gupta, D. Green, W. McMichael, Energ. Fuel. 18 (2004) 569-575.
[9] J. Ren, L.B. Wu, B.G. Li, Ind. Eng. Chem. Res. 51 (2012) 7901-7909.
[10] B.F. Goodrich, J.C. de la Fuente, B.E. Gurkan, Z.K. Lopez, E.A. Price, Y. Huang, J.F. Brennecke, J. Phys. Chem. B 115 (2011) 9140-9150.
[11] Y.T. Liao, S. Dutta, C.H. Chien, C.C. Hu, F.K. Shieh, C.H. Lin, K.C.W. Wu, J. Inorg. Organomet. P. 25 (2015) 251-258.
[12] S. Lee, T.P. Filburn, M. Gray, J.W. Park, H.J. Song, Ind. Eng. Chem. Res. 47 (2008) 7419-7423.
[13] J. Blamey, E. Anthony, J. Wang, P. Fennell, Prog. Energ. Combust. 36 (2010) 260-279.
[14] M. Erans, V. Manovic, E.J. Anthony, Appl. Energ. 180 (2016) 722-742.
[15] A. Perejón, L.M. Romeo, Y. Lara, P. Lisbona, A. Martínez, J.M. Valverde, Appl. Energ. 162 (2016) 787-807.
[16] T. Shimizu, T. Hirama, H. Hosoda, K. Kitano, M. Inagaki, K. Tejima, Chem. Eng. Res. Des. 77 (1999) 62-68.

[17] W. Liu, H. An, C. Qin, J. Yin, G. Wang, B. Feng, M. Xu, Energ. Fuel. 26 (2012) 2751-2767.
[18] J.M. Valverde, J. Mater. Chem. A 1 (2013) 447-468.
[19] M. Alonso, Y. Criado, J. Abanades, G. Grasa, Fuel 127 (2014) 52-61.
[20] J.C. Abanades, G. Grasa, M. Alonso, N. Rodriguez, E.J. Anthony, L.M. Romeo, Environ. Sci. Technol. 41 (2007) 5523-5527.
[21] A. MacKenzie, D. Granatstein, E.J. Anthony, J. Abanades, Energ. Fuel. 21 (2007) 920-926.
[22] M.S. Duyar, M.A.A. Trevino, R.J. Farrauto, Appl. Catal. B: Environ. 168 (2015) 370-376.
[23] J.C. Abanades, E.S. Rubin, M. Mazzotti, H.J. Herzog, Energ. Environ. Sci. 10 (2017) 2491-2499.
[24] R.M. Cuéllar Franca, A. Azapagic, J. CO2 Util. 9 (2015) 82-102.
[25] M. Cai, J. Wen, W. Chu, X. Cheng, Z. Li, J. Nat. Gas. Chem. 20 (2011) 318-324.
[26] M.S. Duyar, S. Wang, M.A. Arellano Trevino, R.J. Farrauto, J. CO2 Util. 15 (2016) 65-71.
[27] Q. Zheng, R. Farrauto, A. Chau Nguyen, Ind. Eng. Chem. Res. 55 (2016) 6768-6776.
[28] S.M. Kim, P.M. Abdala, M. Broda, D. Hosseini, C. Copéret, C. Müller, ACS Catal. 8 (2018) 2815-2823.
[29] X. Peng, K. Cheng, J. Kang, B. Gu, X. Yu, Q. Zhang, Y. Wang, Angew. Chem. Int. Edit. 54 (2015) 4553-4556.
[30] G. Melaet, W.T. Ralston, C.S. Li, S. Alayoglu, K. An, N. Musselwhite, B. Kalkan, G.A. Somorjai, J. Am. Chem. Soc. 136 (2014) 2260-2263.
[31] Y.A. Daza, R.A. Kent, M.M. Yung, J.N. Kuhn, Ind. Eng. Chem. Res. 53 (2014) 5828-5837.
[32] R.V. Gonçalves, L.L.R. Vono, R. Wojcieszak, C.S.B. Dias, H. Wender, E. Teixeira Neto, L.M. Rossi, Appl. Catal. B: Environ. 209 (2017) 240-246.
[33] A. Brennführer, H. Neumann, M. Beller, Angew. Chem. Int. Edit. 48 (2009) 4114-4133.
[34] X.F. Wu, H. Neumann, M. Beller, Chem. Soc. Rev. 40 (2011) 4986-5009.
[35] H. Sun, C.M. Parlett, M.A. Isaacs, X. Liu, G. Adwek, J. Wang, B. Shen, J. Huang, C. Wu, Fuel 235 (2019) 1070-1076.
[36] S. Wang, S. Fan, L. Fan, Y. Zhao, X. Ma, Environ. Sci. Technol. 49 (2015) 5021-5027.
[37] M. Shokrollahi Yancheshmeh, H.R. Radfarnia, M.C. Iliuta, ACS Sustain. Chem. Eng. 5 (2017) 9774-9786.
[38] F. Sadi, D. Duprez, F. Gérard, A. Miloudi, J. Catal. 213 (2003) 226-234.
[39] A.B. Kehoe, D.O. Scanlon, G.W. Watson, Chem. Mater. 23 (2011) 4464-4468.
[40] X. Du, D. Zhang, L. Shi, R. Gao, J. Zhang, J. Phys. Chem. C 116 (2012) 10009-10016.
[41] A. Kambolis, H. Matralis, A. Trovarelli, C. Papadopoulou, Applied Catalysis A: General 377 (2010) 16-26.
[42] V.M. Gonzalez-Delacruz, F. Ternero, R. Pereñíguez, A. Caballero, J.P. Holgado, Applied Catalysis A: General 384 (2010) 1-9.
[43] H. Sun, C. Wu, B. Shen, X. Zhang, Y. Zhang, J. Huang, Mater. Today Sustain. (2018).
[44] E. Santos, C. Alfonsín, A. Chambel, A. Fernandes, A.S. Dias, C. Pinheiro, M. Ribeiro, Fuel 94 (2012) 624-628.
[45] F. Jin, H. Sun, C. Wu, H. Ling, Y. Jiang, P.T. Williams, J. Huang, Catal. Today 309 (2018) 2-10.
[46] H. Roh, I. Eum, D. Jeong, Renew. Energ. 42 (2012) 212-216.
[47] D. Yao, Y. Zhang, P.T. Williams, H. Yang, H. Chen, Appl. Catal. B: Environ. 221 (2018) 584-597.
[48] M. Zhang, Y. Peng, Y. Sun, P. Li, J. Yu, Fuel 111 (2013) 636-642.
[49] H. Guo, X. Kou, Y. Zhao, S. Wang, Q. Sun, X. Ma, Chem. Eng. J. 334 (2018) 237-246.
[50] D. Alvarez, J.C. Abanades, Ind. Eng. Chem. Res. 44 (2005) 5608-5615.
[51] L. Katta, P. Sudarsanam, G. Thrimurthulu, B.M. Reddy, Appl. Catal. B: Environ. 101 (2010) 101-108.
[52] X. Wen, C. Li, X. Fan, H. Gao, W. Zhang, L. Chen, G. Zeng, Y. Zhao, Energ. Fuel. 25 (2011) 2939-2944.
[53] H. Guo, J. Feng, Y. Zhao, S. Wang, X. Ma, J. CO2 Util. 19 (2017) 165-176.
[54] H. Lu, A. Khan, S.E. Pratsinis, P.G. Smirniotis, Energ. Fuel. 23 (2008) 1093-1100.
[55] A. Antzara, E. Heracleous, A.A. Lemonidou, Appl. Energ. 156 (2015) 331-343.
[56] M.L. Granados, A. Gurbani, R. Mariscal, J. Fierro, J. Catal. 256 (2008) 172-182.
[57] Z. Fang, B. Yuan, T. Lin, H. Xu, Y. Cao, Z. Shi, M. Gong, Y. Chen, Chem. Eng. Res. Des. 94 (2015) 648-659.
[58] D. Li, Y. Gong, Y. Zhang, C. Luo, W. Li, Q. Fu, C. Pan, Sci. Rep. 5 (2015) 12903.
[59] L. Liu, H. Zhang, J. Yang, Y. Mu, Y. Wang, J. Mater. Chem. A 3 (2015) 22393-22403.
[60] J. Xiao, S. Yang, J. Mater. Chem. 22 (2012) 12253-12262.

[61] M. Broda, A.M. Kierzkowska, C.R. Müller, Environ. Sci. Technol. 46 (2012) 10849-10856.
[62] S. Wu, Y. Zhu, Ind. Eng. Chem. Res. 49 (2010) 2701-2706.
[63] A. Ranjbar, A. Irankhah, S.F. Aghamiri, J. Environ. Chem. Eng. 6 (2018) 4945-4952.
[64] L. Wang, H. Liu, Y. Chen, S. Yang, Int. J. Hydrogen Energ. 42 (2017) 3682-3689.
[65] S. Hilaire, X. Wang, T. Luo, R. Gorte, J. Wagner, Applied Catalysis A: General 215 (2001) 271-278.
[66] R. Gorte, S. Zhao, Catal. Today 104 (2005) 18-24.
[67] Y. Liu, Z. Li, H. Xu, Y. Han, Catalysis Communications 76 (2016) 1-6.
[68] G. Jacobs, L. Williams, U. Graham, D. Sparks, B.H. Davis, J. Phys. Chem. B 107 (2003) 10398-10404.
[69] G. Jacobs, E. Chenu, P.M. Patterson, L. Williams, D. Sparks, G. Thomas, B.H. Davis, Applied Catalysis A: General 258 (2004) 203-214.
[70] G. Jacobs, U.M. Graham, E. Chenu, P.M. Patterson, A. Dozier, B.H. Davis, J. Catal. 229 (2005) 499-512.
[71] A. Goguet, F.C. Meunier, D. Tibiletti, J.P. Breen, R. Burch, J. Phys. Chem. B 108 (2004) 20240-20246.